MTLA 39 (2025) 102363

Contents lists available at ScienceDirect

Materialia

journal homepage: www.elsevier.com/locate/mtla

Full Length Article

Friction Stir welding effects on the corrosion resistance of the 2098-T351 alloy

João Victor de S. Araujo [a,*], Mariana X. Milagre [a], José Wilmar Calderón-Hernández [b], Nathanael W. Morais [a], Isolda Costa [a]

[a] Instituto de Pesquisas Energéticas e Nucleares, IPEN/CNEN, Av. Prof. Lineu Prestes, 2242, São Paulo, Brazil
[b] Grupo de Investigación Ingeniar, Facultad de Ciencias Básicas e Ingenierías, Corporación Universitaria Remington, Calle 51 #51-27, Medellín, Colombia

ARTICLE INFO

Keywords:
Al-Cu-Li alloy
Friction stir welding
Microstructure
Localized corrosion

ABSTRACT

The effects of friction stir welding (FSW) on the corrosion resistance of the AA2098-T351 aluminum alloy were investigated through immersion and electrochemical tests in a 0.005 mol L^{-1} NaCl solution. The findings revealed that the welding joint (WJ), which includes the thermomechanically affected zone (TMAZ) and stir zone (SZ), demonstrated superior localized corrosion resistance compared to the HAZ and BM. The SZ and TMAZ demonstrated cathodic behavior relative to the HAZ and BM. Furthermore, the differences in corrosion resistance among the isolated welding zones and their behavior under galvanic coupling were analyzed and discussed, highlighting the complex electrochemical interactions within the welded structure.

1. Introduction

Friction stir welding (FSW) is a solid-state process that allows the joining of materials difficult to weld (such as aluminium alloys) due to their physical properties [1–3]. The FSW process generates distinct zones with varied microstructures and properties due to combined thermal and mechanical effects. The process involves the rotation of a pin, generating frictional heat to facilitate welding. The main zones created by the process are known as stir zone (SZ), thermomechanically affected zone (TMAZ), heat affected zone (HAZ). The zone not affected by FSW is the base metal (BM). The SZ is characterized by intense heating and plastic deformation that lead to dynamic recrystallization with fine grains and dissolution of the primary strengthening phase in the BM. The TMAZ is the area where the tool rotation causes deformation and heating, as a consequence, dissolution of the primary strengthening phase is also observed, and the grains are elongated by deformation. The HAZ is the zone affected by thermal cycles along the welded material, leading to the partial dissolution and coarsening of precipitates. Finally, the base metal (BM) corresponds to the zones that are not affected by the welding process [1–12].

The zones of different microstructures generated by FSW exhibit different electrochemical reactivities [13–20]. However, there is no agreement in the literature concerning the zones most susceptible to corrosion. Bousquet et al. [13], showed that in the case of the 2024-T3 alloy, corrosion attack occurred mainly in the HAZ close to the TMAZ, although in the TMAZ some grain boundaries were attacked, and few pits were detected. Additionally, pitting corrosion and isolated intergranular corrosion (IGC) zones were observed in the SZ. The preferential location of S' phase in the grain boundaries increased the susceptibility of the HAZ/TMAZ interface to IGC. Jariyaboon et al. [15] showed that localization of anodic and cathodic areas is dependent on welding parameters. For instance, they reported intergranular attack in the SZ for low rotation speed, whereas, for high rotation speed, corrosion attack occurred in the HAZ of the same alloy. According to Kang et al. [21]., the HAZ in the 2219-T8 Al-Cu alloy is the zone most susceptible to corrosion. For the Al-Cu-Li 2195 alloy, higher pitting resistance was associated with the SZ compared to the BM [14,18]. Proton et al. [20] reported that the SZ of the AA2050 welded by FSW was susceptible to intergranular and intragranular corrosion. Zhang et al. [22] studied the 2A97 Al-Cu-Li and found a high population of T1 phase (Al_2CuLi) precipitates in the TMAZ, which was associated with the high susceptibility of this zone to localized corrosion. The corrosion susceptibility of different aluminum alloys welded by FSW largely depends on their composition, welding parameters, and the resulting microstructure. Therefore, it is not possible to generalize the effects of FSW across different aluminum alloys.

Electrochemical techniques have been largely used to evaluate the reactivity of zones affected by FSW [16,20,23–30]. Using

* Corresponding author.
E-mail address: jvaraujo@alumni.usp.br (J.V.S. Araujo).

https://doi.org/10.1016/j.mtla.2025.102363
Received 8 December 2024; Accepted 3 February 2025
Available online 8 February 2025

electrochemical impedance spectroscopy (EIS), Peng Yong et al. [25] showed that the polarization resistance of the 6082-T6 alloy welded by FSW was superior to that of MIG joint and the base metal. Davoodi et al. [26] applied EIS [31] on corrosion characterization of dissimilar alloys, specifically AA5083 and AA7023, and found intermediate corrosion resistance for the weld when it was compared with the BM of the alloys 5083 (higher resistance) and 7023 (less resistance). Furthermore, De Abreu et al. [16], in an electrochemical study of dissimilar Al alloys (2024 and 7075) reported lower impedances associated with the FSW affected zones compared to the two aluminum alloys unaffected by the welding process, that is, the base metal (BM).

Galvanic coupling effect has been studied by local electrochemical techniques [16,22,25,27]. According to the literature, galvanic coupling can be detected by local electrochemical impedance spectroscopy (LEIS) in welded alloys [16,24]. Donatus et al. [28]. showed galvanic coupling between dissimilar aluminium alloys, specifically AA5083 and AA6082, by means of open circuit potential (OCP) measurements. Bertoncello et al. [27] used scanning vibrating electrode technique (SVET) to study the corrosion mechanisms of dissimilar alloys (2024 and 7050) and to identify the cathodic and anodic zones. The authors found that the border between both alloys in the SZ at OCP was the most susceptible region to local attacks due to the intense galvanic coupling in this contact region.

Despite extensive studies on the effects of friction stir welding (FSW) on aluminum alloys, the corrosion mechanisms of Al-Cu-Li alloys, such as AA2098-T351, remain poorly understood. In particular, the correlation between microstructural changes induced by FSW and localized corrosion behaviors in the different zones (BM, HAZ, TMAZ, and SZ) has not been thoroughly investigated. Most published studies focus on microscopic analyses, while the comprehensive evaluation of corrosion resistance across the weld zones using electrochemical techniques remains scarce. Additionally, the corrosion behavior of this alloy is not well established, and no prior studies have specifically addressed the effects of FSW on the corrosion resistance of AA2098-T351.

The microstructural features and, consequently, the corrosion behavior of FSW-welded alloys depend on the welding parameters [15], which make each process unique. This investigation aims to elucidate the correlation between the microstructure of the AA2098-T351 and its corrosion resistance through a combination of electrochemical techniques and microscopic methods.

2. Material and methods

2.1. Material

AA2098-T351 plates (3.4 wt% Cu, 1 wt% Li, 0.3 wt% Mg, 0.3 %wt Ag, 0,4 wt% Zr, 0.04 wt% Fe, 0.05 wt% Si, 0.02 wt% Zn, 0.003 wt% Mn) were used in this work. Optical microscopy micrographs (top view) of the AA2098-T351 welded by FSW used in this study are shown in Fig. 1.

2.2. Friction stir welding (FSW)

FSW process was performed using a rotation speed of 700 rpm, a transverse speed of 300 mm/min and a load in the range of 8 kN – 15 kN. An H13 steel tool with a 16 mm diameter shoulder and a 3.2 mm long adjustable pin, matching the plate thickness, was used. Thermocouples were attached underneath the plate, at distances of 6 mm, 9 mm and 12 mm from the center of the joint to obtain the thermal profile and to perform simulations referring to the temperature profile. Thermal simulations were performed using the finite element COMSOL v5.2 software. The physical phenomena in welding, such as heat transfer by conduction and radiation, were considered. The welding model counted 86,009 elements. The measurements obtained by the thermocouples were used as input data for the calibration of the thermomechanical model. Further details regarding the thermal simulation can be found in our previous work [32].

2.3. Surface preparation

All the tests were carried out on samples sequentially polished to a 1 μm surface finish. Silicon carbide papers and diamond pastes were employed for this purpose. After polishing, the samples were degreased, rinsed with deionized water, and dried using a hot air stream.

2.4. Conventional electrochemical techniques

The electrochemical characterization of each welded zone, Fig. 2, was carried out by anodic and cathodic polarization and electrochemical impedance spectroscopy (EIS).

The BM measures were carried out on samples from an unwelded plate. Each experiment was repeated thrice to ensure reproducibility. Polarization curves were obtained using an AUTOLAB PGSTAT potentiostat controlled by NOVA 1.11 software. The tests were performed at room temperature using a three electrode-cell setup with $Ag/AgCl_{KCl(sat)}$ as a reference electrode and a platinum wire as counter electrode. The

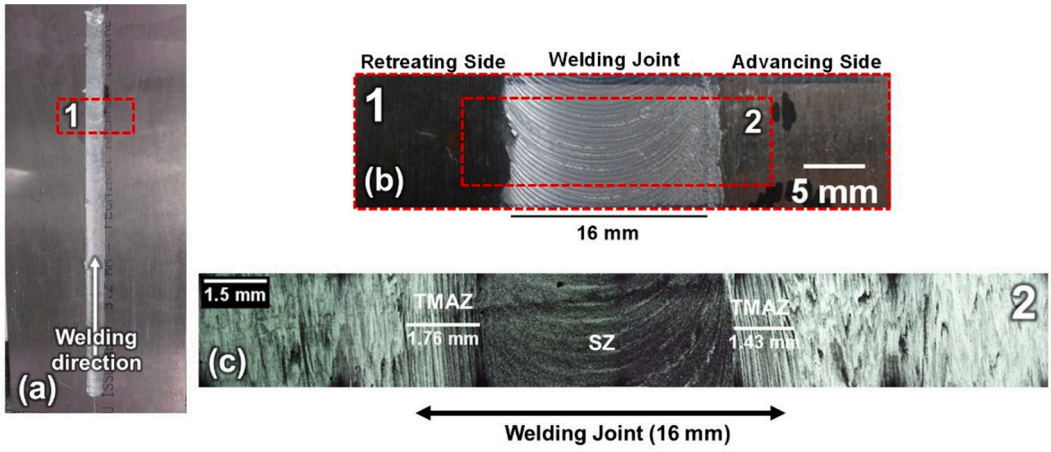

Fig. 1. . Optical macrographs and microscopy of a 2098-T351 aluminum plate welded by friction stir welding (FSW), highlighting the welding joint dimensions and the locations of the retreating side (RS) and advancing side (AS): (a) macrograph of the entire plate showing the welding direction and joint; (b) detailed macrograph of the red dashed square in (a), illustrating the welding joint dimensions (16 mm) and sides (RS and AS); and (c) optical microscopy of the weld, showing the distinct welding zones, including the stir zone (SZ) and thermomechanically affected zone (TMAZ), with their respective thicknesses.

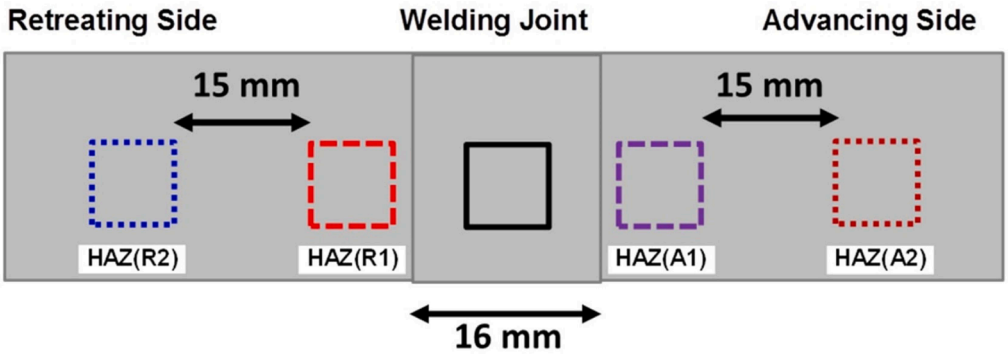

Fig. 2. . Schematic diagram of the regions of the weldment exposed to 0.005 mol l^{-1} of NaCl solution for electrochemical tests.

exposed surface of the working electrode was 5 × 5 mm^2 The identification of the welding zones analyzed were based on the microstructural observations, microhardness profile, tool dimensions and thermal profile[32]. The welding zones were individually masked using beeswax. Anodic polarization curves were obtained from the open circuit potential (OCP) to 0.4 V vs. $Ag/AgCl_{KCl(sat)}$ and the cathodic ones from OCP to −1.3 V vs. $Ag/AgCl_{KCl(sat)}$, with a scan rate of 1 mV/s. The electrolyte used for the tests was 0.005 mol. l^{-1} NaCl solution at (22 ± 2) °C. EIS data was obtained potentiostatically at the OCP in the frequency range of 10 kHz to 10 mHz with 10 mV amplitude signal and an acquisition rate of 10 points per decade, using an AUTOLAB PGSTAT potentiostat controlled by NOVA 1.11 software.

2.5. Scanning vibrating electrode technique (SVET)

Scanning Vibrating Electrode Technique (SVET) was used to evaluate localized corrosion in the friction stir welded (FSW) regions of the AA2099-T351 alloy. The welded zones were isolated using beeswax resin to confine the electrolyte contact area. The SVET probe, positioned at 100 ± 3 μm above the surface, employed a platinum microelectrode (~15 μm in diameter) vibrating at optimized amplitudes and frequencies (~19 μm, 174 Hz in X, and 73 Hz in Z).

Measurements were conducted in a 0.005 mol L^{-1} NaCl solution, a low concentration that allows better visualization of the initial stages of corrosion and minimizes the interference of corrosion product accumulation. The system was calibrated before each test to ensure accuracy. Current density maps were generated over a defined grid (35 × 25 points) to analyze localized anodic and cathodic activity. The corrosion evolution was monitored over 12 h, with SVET maps acquired at regular intervals to assess the susceptibility and progression of corrosion in the FSW zones.

2.4. Immersion test

Immersion tests were performed to evaluate the overall corrosion morphology and the severity of localized attacks in each weld zone. Samples were prepared by sequential polishing to a 1 μm surface finish and were immersed in naturally aerated 0.005 mol/L NaCl solution at room temperature (~22 °C) for 24 h.

After immersion, the samples were removed, rinsed with deionized water, dried with a hot air stream, and analyzed using optical microscopy (OM) and scanning electron microscopy (SEM). The surface analysis focused on the identification of localized corrosion features such as severe localized corrosion (SLC), pitting, trenching around micrometric particles, and intergranular corrosion (IGC).

The lower concentration of 0.005 mol/L NaCl solution was selected to simulate early-stage corrosion processes and allow a detailed evaluation of corrosion mechanisms. The slower reaction kinetics facilitated the observation of differences between the BM, HAZ, TMAZ, and SZ, highlighting the role of microstructural changes caused by FSW.

2.5. Gel visualization test

Gel visualization test [16] test was conducted to evaluate the localized corrosion behavior of the welded zones in the AA2098-T351 alloy. The gel was prepared by dissolving 3 g of agar-agar in 100 mL of boiling 0.6 mol/L NaCl solution, with 7 mL of a universal pH indicator added to the mixture. The prepared gel was poured onto metallographically polished samples immediately after preparation to prevent premature drying, which could interfere with the test. To ensure uniform exposure, the edges of the samples were coated with an insulating varnish to avoid side reactions.

The samples were monitored for up to 4 h under ambient conditions, and the color changes in the gel were used to identify anodic and cathodic regions across the welded zones. Anodic areas were associated with acidic pH (color changes to red), whereas cathodic regions corresponded to alkaline pH (color changes to green or blue). This method was chosen to highlight localized pH changes caused by corrosion reactions in the BM, HAZ, TMAZ, and SZ.

The use of a 0.6 mol/L NaCl solution in this test was intended to accelerate corrosion processes and enhance the visibility of localized corrosion sites. The higher salt concentration increased ionic conductivity and promoted faster electrochemical reactions, facilitating the identification of anodic and cathodic zones. Starting the test promptly after pouring the gel is critical to initiate the reaction before the gel begins to dry.

2.6. Microstructural characterization and microhardness

Optical microscopy was used for surface observation, and for this, the microstructural features were revealed by etching in a solution composed of 2 % HF and 25 % HNO_3. Scanning electron microscopy (SEM) images were also acquired using a Hitachi TM 3000 microscope with an incident beam of 15 keV. Transmission Electron Microscopy (TEM) was used to study the distribution and characteristics of phases in the AA2098-T351 alloy. Thin foils with a diameter of 3.0 mm were prepared by mechanical polishing followed by electropolishing at 20 V in a solution of 30 % nitric acid in methanol. Selected area diffraction (SAD) patterns were obtained during the TEM analysis to identify and confirm the crystallographic phases present in the different welding zones. The diffraction patterns were used to confirm the morphology, orientation, and spatial distribution of these phases across the zones, including the BM, HAZ, and SZ. The results from these analyses were correlated with previous studies conducted by our research group [32], which investigated the microstructural evolution of the AA2098-T351 alloy during Friction Stir Welding (FSW). These studies provide a foundation for understanding the distribution of phases and their relationship to mechanical and corrosion behavior. TEM samples were prepared using a TenuPol equipment. The imaging was carried out using a JEOL 2100 microscope. Microhardness measurements were also used to correlate the microstructural modifications by the FSW process with

the electrochemical results. The measures were carried out in a Knoop/Vickers Tukon 1202 Wilson Hardness at the sample surface in steps of 0.2 mm using a load of 200 gf for 10 s.

3. Results and discussion

3.1. Microstructural characterization

As previously mentioned, the FSW process generated four different welding zones characterized by microstructural modifications. These modifications occur at nanometer and micrometer scales and result in different reactivity along the welded material. In our previous work, the FSW effect on the microstructure and mechanical behaviour of the AA2098-T351 Al-Cu-Li alloy was investigated [29,32]. Microhardness test, differential scanning calorimetry (DSC) tests and TEM characterization provide information about nano-sized phase distribution in this alloy. However, it is important to emphasize that the T1 phase is the most deleterious phase responsible for the decrease in corrosion resistance of the Al-Cu-Li alloys.

Fig. 3 shows the T1 phase distribution across the AA2098-T351 welded sample.

In the BM, the T1 phase was distributed inside the grains, Fig. 3a. In the base metal (BM), the T1 phase is uniformly distributed inside the grains, as observed in Fig. 3a. These precipitates contribute significantly to the mechanical properties of the BM but are also highly susceptible to severe localized corrosion (SLC), as discussed in our previous study [32]. TEM images revealed edge-on variants of the T1 phase, depending on the grain orientation. In the [110] zone axis (ZA), two of four T1 variants appear as straight lines along ⟨111⟩ directions (Fig. 3b), while in the [112] ZA, only one variant is visible (Fig. 3c).

The heat-affected zone (HAZ) exhibits a different behavior due to the thermal effects of welding, as shown in Fig. 4.

The T1 phase in this zone is smaller, coarser, and primarily distributed along the grain boundaries (Fig. 4a). The partial dissolution of the T1 phase in the HAZ is consistent with DSC results from our prior work [32], which showed a reduction in T1 content and an increase in δ′ precipitation due to lithium redistribution. These thermal effects lead to a decrease in microhardness in the HAZ compared to the BM.

In the thermo-mechanically affected zone (TMAZ), the microstructure depends on the thermal and mechanical gradients during welding. TEM analysis of the TMAZ, as shown in Fig. 5, revealed that the retreating side (RS) contained a higher density of T1 precipitates compared to the advancing side (AS). In the TMAZ/HAZ-RS (Fig. 5a), weak T1 intensities were observed along the ⟨111⟩ direction, primarily decorating the grain boundaries. On the TMAZ/HAZ-AS (Fig. 5b), no evidence of T1 phase was detected, which is consistent with the lower microhardness observed on the AS. This asymmetry reflects the differences in thermal exposure between the RS and AS, as reported in our earlier studies [32].

Finally, the stir zone (SZ) presents the most significant modifications due to the high temperatures and intense plastic deformation inherent to FSW. A low density of T1 precipitates is observed in the SZ (Fig. 5c), as most of the T1 phase dissolves during welding. Other phases, such as δ′ and T2 (Al_5Li_3Cu), precipitate during cooling. The low density of T1 phase in the SZ aligns with the DSC thermograms from previous studies [32], which show pronounced peaks associated with Guinier-Preston (GP) zone dissolution. The dynamic recrystallization and grain refinement in the SZ contribute to its higher microhardness compared to the TMAZ.

These observations highlight the significant impact of the FSW process on the distribution and morphology of the T1 phase in the different welding zones. The asymmetric temperature profiles and strain gradients between the advancing and retreating sides result in notable differences in microstructure, which correlate with the mechanical properties and corrosion resistance of the welded material, as detailed in our previous work [32].

Micrometric particles also play a significant role on the corrosion behavior of Al alloys. Fig. 6 shows the distribution of micrometric particles in the different welding zones.

In BM and HAZ, the micrometric particles are mainly distributed according to the deformation direction, while in the SZ, these particles are smaller and evenly distributed due to pin rotation effects leading to breaking of particles and their spread across the tool domain. The effects of micrometric particles on the corrosion of Al alloys are mainly related to their different electrochemical activities (with respect to the matrix) which are associated with their different composition [33–35]. EDX analysis was carried out on the various particles and the matrix of each zone. A total of 30 particles in each zone was characterized, and the results are shown in Fig. 7.

Fig. 7e-f show no differences between the composition of the particles irrespective of the welding zone. The typical compositions of the particles, Fig. 7g-h, were found to be Al-Cu-Fe and Al-Cu, thus cathodic in relation to the matrix [33,34]. Traces of Ag were found; however, the values are in the limit of the equipment detection.

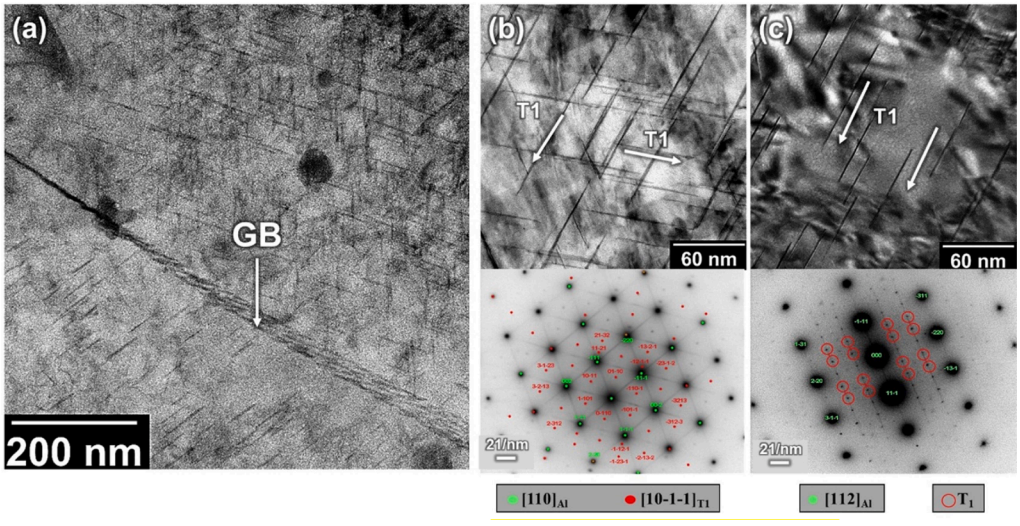

Fig. 3. . (a-c) TEM bright field images and selected area diffraction (SAD) patterns obtained in [110] and [112] orientations showing T1 phase distribution in the BM. The white arrow in (a) indicates the grain boundary (GB).

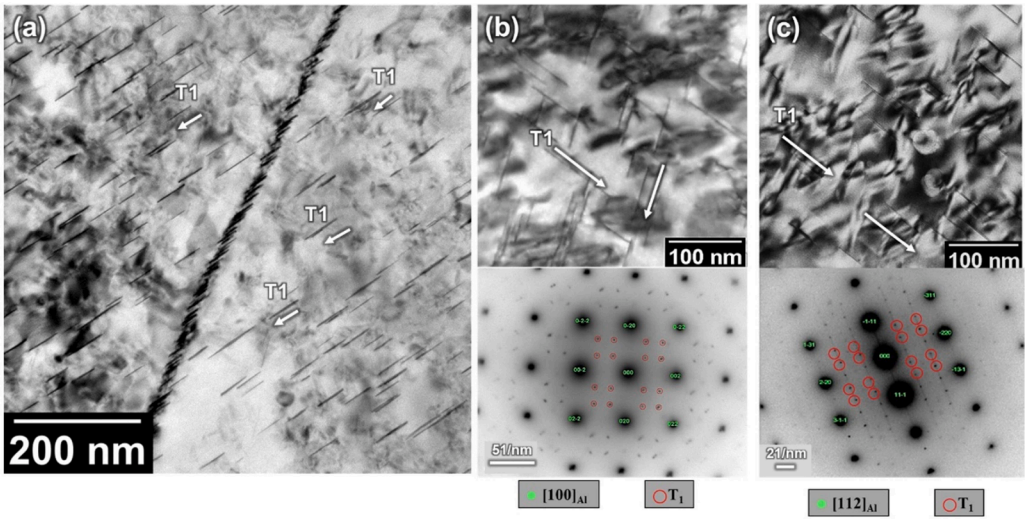

Fig. 4. . (a-c) TEM bright field images and selected area diffraction (SAD) patterns obtained in [110] and [112] orientations showing T1 phase distribution and variants in the HAZ.

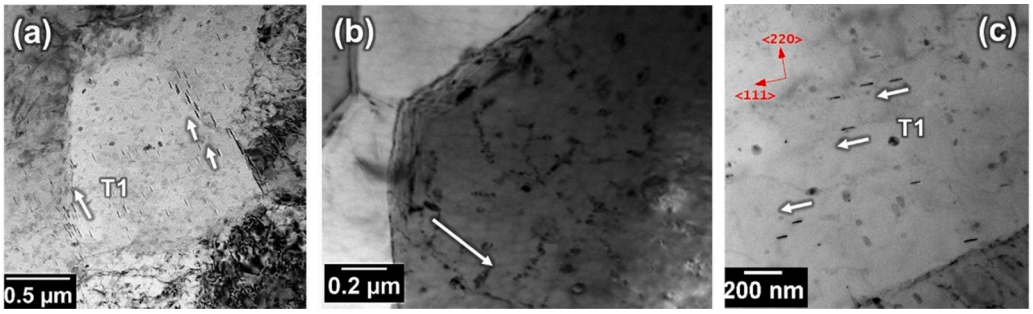

Fig. 5. . TEM bright field images showing T1 phase distribution and variants in the welding joint. (a) TMAZ/HAZ of RS; (b) TMAZ/HAZ of AS; (c) SZ.

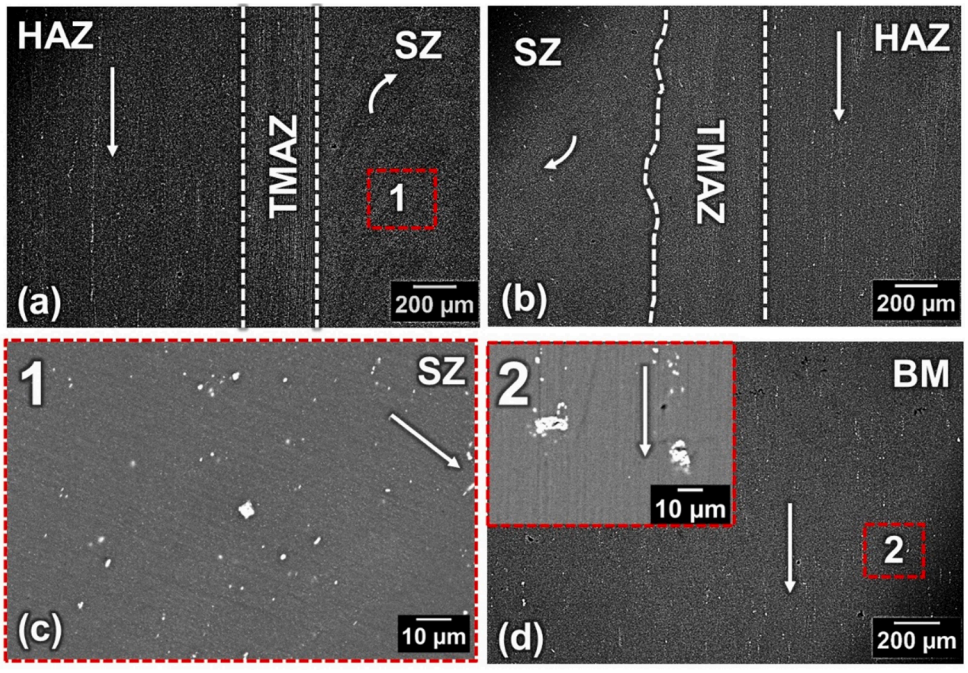

Fig. 6. . SEM images of different welding zones showing the micrometric particle distribution. (a) Retreating side; (b) Advancing side; (c) High magnification of the SZ region; (d) BM micrometric particles distribution.

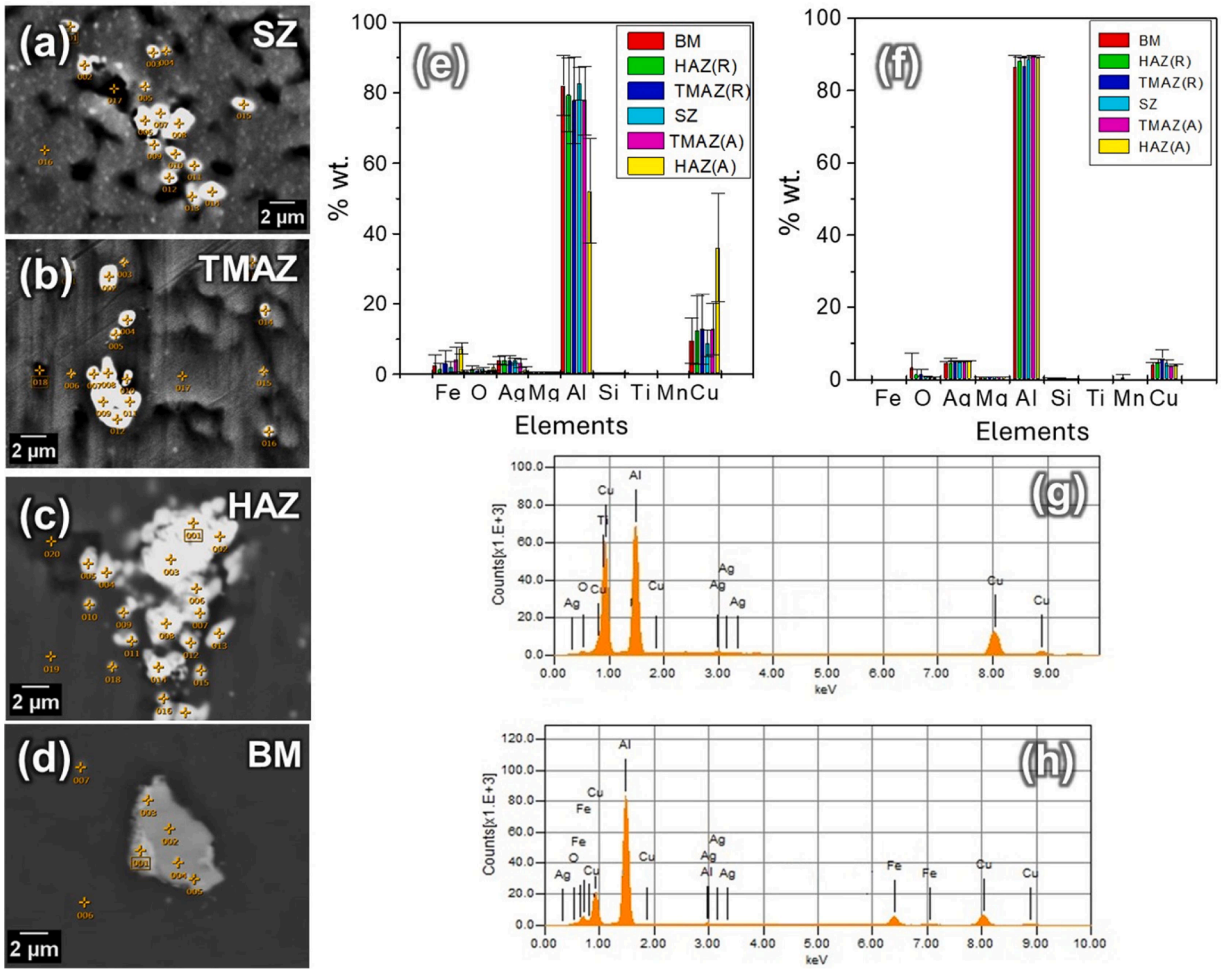

Fig. 7. . (a-d) Typical micrometric particles at different welding zones (c) Average composition of the Al-Cu-Fe-(Ag); (b) Average composition of the Al-Cu-(Ag); (c-d) Typical EDX spectra of the micrometric particles.

3.2. Corrosion characterization

Different corrosion mechanisms were observed in the weld exposed to 0.005 mol·L^{-1} of NaCl solution for 24 h. Fig. 8 shows the features of the attack in the BM.

Surface observation after the immersion test revealed the presence of severe localized corrosion (SLC) in the regions indicated as 1, 2 and 3. The high activity of these regions led to the accumulation of corrosion products in region 2, and to rings around the SLC corresponding to cathodically protected areas associated with deep attack in the anodic regions. At the SLC sites, the amount of T1 phase was very high. Fig. 9 shows SLC where an intragranular attack was observed, Fig. 9a, and a crystallographic attack.

The relationship between the T1 phase density and the SLC has been reported [22,34]. As previously mentioned, T1 phase is the main hardening phase in Al-Cu-Li alloys and that is mostly related to SLC [36,37]. According to literature [38,39], the corrosion mechanism associated with the T1 phase starts with the preferential dissolution of lithium from this phase, leading to copper enrichment and, subsequently, inversion of polarity with respect to the matrix. As previously observed by TEM analysis, the T1 phase is evenly distributed inside the grains leading to intragranular attack. Fig. 9a confirms this observation, showing a preserved grain boundary in a region of SLC. Moreover, because of the temper condition of studied alloy (T351), which comprises a stretching step before natural aging, attacks orientated along preferential directions were also observed, as Fig. 9b shows. The stretching step in Al-alloys is used to relieve stress. However, it also creates regions of high dislocation densities that are preferential sites for T1 phase precipitation during aging steps. Consequently, during immersion in corrosive solutions, the regions of large amounts of T1 phase, act as preferential sites for corrosion attack and result in the aligned attack morphology observed [33,34]. Cavities and trenching are also observed in the attacked surface, region 4. The development of these cavities is associated with micrometric particles. As reported earlier [35], these particles contain Al, Fe, Cu also play an essential role in the corrosion of this alloy. Fig. 10 shows EDX maps of attacked micrometric particles.

The results indicate a decrease in Al content and an increase in Fe and Cu, suggesting cathodic element enrichment, which subsequently leads to trenching of the surrounding matrix. Eventually, detachment of the particles occurs, and cavities are formed. Moreover, the EDX maps also show Cu and Ag deposition (white arrows). The Cu and Ag particles are deposited preferentially at the vicinity of the micrometric particles (Fig. 10a-b), in the SLC sites, Fig. 10e-f. Cu and Ag deposition promotes cathodic reactions stimulating the local dissolution of the matrix in their surroundings. The Cu redeposition mechanism is reported because of detachment of Cu rich particles that are oxidized in the solution and subsequently re-deposited on the aluminium alloy surface promoting the continuity of attack by increasing the cathodic activity at the deposition sites [40–43]. Ag is an alloying element added to Al-Cu-Li alloys to promote the uniform dispersion of T1 phase in the matrix [44,45]. According to Murayama et al. [45], the T1 phase is associated with Ag atoms that are segregated at the T1/α interfaces rather than being incorporated within the precipitate. Segregation of Ag at the Ω/α interfaces has also been reported by other authors [44]. Thus, because the

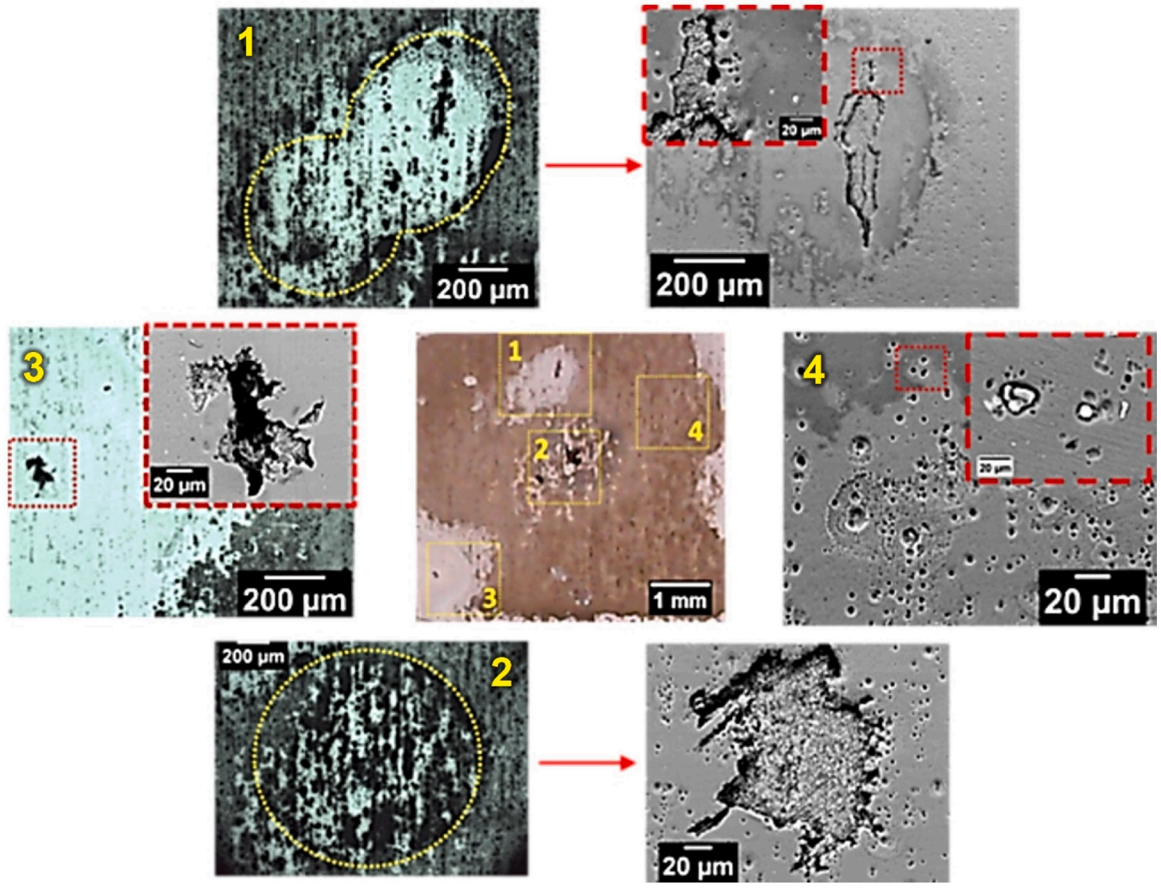

Fig. 8. . Features of the surface attack of the base metal (BM) of AA2098-T351 Al-Cu-Li alloy after 24 h of immersion in 0.005 mol l^{-1} of NaCl.

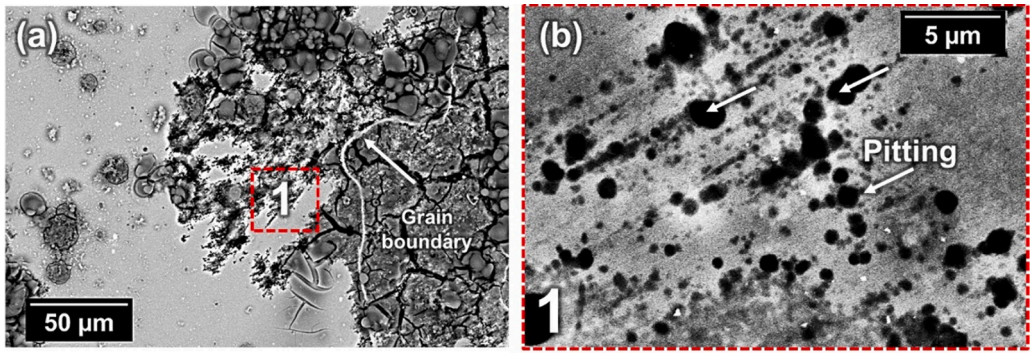

Fig. 9. . (a) Intragranular attack and (b) aligned attack in the SLC sites of AA2098-T351 Al-Cu-Li alloy immersed in 0.005 mol l^{-1} of NaCl during 24 h.

relationship between Ag and T1 phase precipitation the redeposition of Ag might occur on the SLC attack vicinity.

Results from immersion tests for welded samples showed that the FSW process modifies the corrosion morphology across the surface of the welded sample, Fig. 11.

Different behaviors were associated with the various microstructures resulting from the welding process. Differences in T1 phase distribution across the weldment was previously reported by TEM analysis, Figs. 3-5. In the HAZ, Fig. 11b, a small volume of coarse T1 phase was observed, and, also, the corrosion attack at either side, AS and RS, was modified, as shown in Fig. 11b. Intragranular attack related to SLC sites is still present in these zones. In addition, intergranular corrosion (IGC) was also observed and related to the smaller volume of coarsened T1 phase precipitated at the GB, compared to the BM. Cavities and trenching associated with the micrometric particles were also observed. In the welding joint (SZ and TMAZ), the T1 phase was rarer. In this region, temperatures ranging from 300 °C to 600 °C were reached, Fig. 11a. This resulted in the dissolution of T1 phase and favored the precipitation of the δ' (Al_3Li), while Cu remained in solid solution. Precipitation of phases as T2 (Al_5Li_3Cu) or TB ($Al_{7.5}LiCu_4$) also can be favored by the FSW process [46]. The effect of these microstructural variations in the TMAZ is shown in Fig. 11(c-e), where trenching and copper enriched discontinuous oxide products were found. Again, cavities and trenching related to micrometric particles were seen in this zone.

Results from the agar-agar visualization test, Fig. 12, provided additional information on the reactivity of the different weld affected zones in the 2098-T351alloy.

According to this figure, galvanic coupling is established between the welding joint (TMAZ and SZ) and the HAZ. After 1 h of test, a green area was seen at the center of the sample. As time progressed, the anodic and

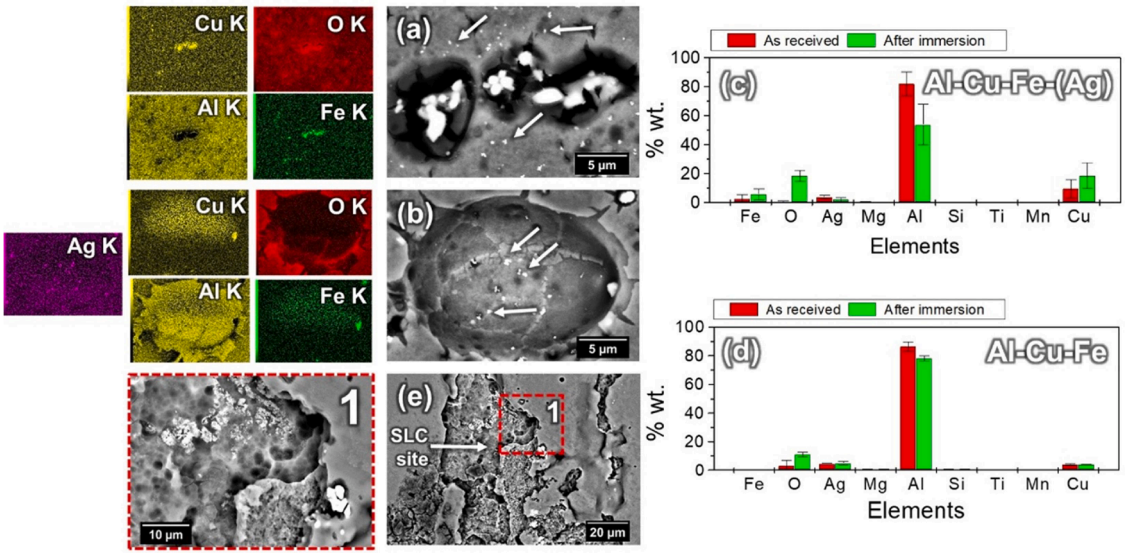

Fig. 10. . EDX maps of corrosion sites associated with the micrometric particles of AA2098-T351 Al-Cu-Li alloy immersed in 0.005 mol l^{-1} ^{1} of NaCl for 24 h. (a) trenching regions; (b) cavities regions; (c-d) Composition variation of the micrometric particles before and after immersion. (e-f) Cu re-deposition at the SLC sites.

cathodic zones became increasingly separated and were clearly identified with the SZ and TMAZ being cathodic to the HAZ and BM. This test showed higher SLC resistance in the SZ and TMAZ compared to the HAZ and BM. The high temperatures reached in the SZ and TMAZ zones, leading to partial dissolution to T1 phase and decreases susceptibility to SLC. On the other hand, in the HAZ where lower temperatures (< 200 °C) were reached and in the BM, the T1 phase is present in high density and the SLC was pronounced. In the anodic areas, acidification occurs due to hydrolysis stimulated by metallic cations, whereas in the welding joint region oxygen reduction occurs. In the welding joint corrosion was observed despite the fact that it was predominantly cathodic relative to the HAZ and BM (Fig. 11). The observed corrosion, in the SZ, which is not severe, results from chemical attack around the micrometric particles due alkalinization [47]. However, at the BM and HAZ the T1 particle is the main culprit. This result reinforces the indication that T1 is the phase mainly responsible for the severe localized corrosion leading to pH modifications in the agar gel test.

3.3. Electrochemical characterization

The anodic polarization curves of the BM and welding join (WJ) after 30 min of immersion in 0.005 mol. l^{-1} NaCl solution are shown in Fig. 13.

In order to compare the welding zones corrosion resistance and the currents densities were taken from the same overpotential (50 mV). It was observed to be lower current for the WJ. Higher current densities were recorded for the BM due to the high susceptibility to SLC associated with this zone. In addition, the relatively smaller currents obtained for the WJ are related to the lower amounts of T1phase in this region. The tested surfaces showed different features associated with the anodic sites, Fig. 13b-c. Only intergranular corrosion (IGC) and pits were associated with the SLC in the WJ, while intragranular corrosion was observed in the SLC sites of the BM. In addition, a larger number of anodic sites compared to WJ were seen on the BM.

The cathodic polarization curves, Fig. 14, show that diffusion controls the reduction reactions.

A slight difference between both the SZ and the BM was observed. In contrast to the anodic polarization curves, higher cathodic currents were observed for the SZ compared to the BM. Fig. 14b-c show a representative surface of the SZ and BM respectively, where it is possible to see more activated areas related to the micrometric particles on the SZ. The micrometric particles are formed during the casting process. Thus, in the welding process, these particles are broken up by the tool movement and are also uniformly distributed increasing the cathodic surface and, consequently, the cathodic currents in this zone.

Fig. 15 shows the surface of each weld zone after the EIS analysis.

Different from the results obtained for galvanically coupled zones, Fig. 10, when the weld affected zones are tested in isolation, all the zones showed SLC. In the WJ, Fig. 12a, SLC was related to IGC, as shown after anodic polarization test. In BM and HAZ, intragranular corrosion was the main type of attack observed, Fig. 12c.

Fig. 16 compares EIS diagrams of the following zones: WJ, HAZ (1 and 2) and BM.

The stability of the system was assessed using the OCP curves obtained 15 min before the tests. Despite the distinct morphologies of attack observed, the EIS results revealed only minor differences among the tested zones. The EIS diagrams consistently identified three time-constants across all regions: the first, in the frequency range of 100–10 Hz, corresponds to the presence of residual oxides on the surface; the second, between 10 and 1 Hz, is associated with the charging of the double layer coupled to charge transfer resistance; and the third, at lower frequencies, relates to a diffusion-controlled process, aligning with the cathodic polarization results [37,48].

The WJ region exhibited higher impedance values due to the reduced amount of T1 phase, which dissolves during the FSW process. Conversely, the HAZ presented the lowest resistance, attributed to the coarsened and smaller T1 phase and the presence of larger precipitate-free zone (PFZ) compared to BM. These observations indicate a clear relationship between the electrochemical and mechanical behaviors of Al-Cu-Li alloys.

Nyquist plots further highlighted that the WJ region had superior corrosion resistance, as evidenced by the higher peak and larger capacitive arc (Fig. 16b). Additionally, in logarithmic scale impedance plots, this region demonstrated better corrosion resistance, with slightly elevated curves relative to the other weld zones (Fig. 16c). On the other hand, the BM region displayed higher resistance when the impedance modulus (|Z|) was plotted against frequency, showing slightly elevated values in the Nyquist diagram (Fig. 16b).

The HAZ region, however, had the lowest peak, which can be attributed to challenges in isolating the electrochemical cell in this area. This region is prone to galvanic pair formation, intensifying the corrosion process. Metallurgical transformations in the thermally affected zones, such as grain refinement and the development of less noble phases, promote the formation of micro-galvanic cells, exacerbating corrosion activity [32,48].

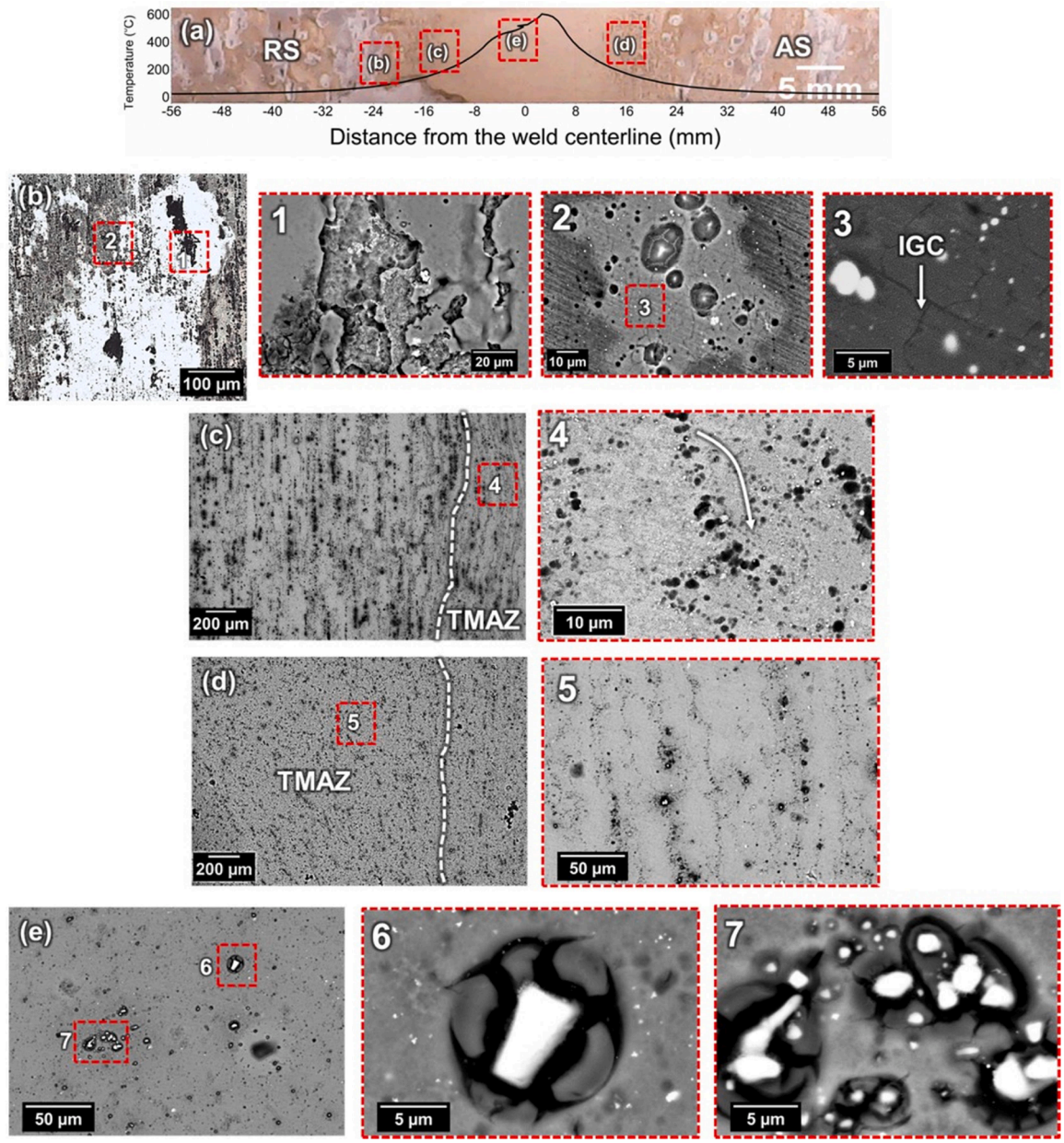

Fig. 11. . (a) Relationship between the corrosion mechanism and thermal profile over the welded sample immersed in 0.005 mol l^{-1} [1] of NaCl for 24 h; (b) corrosion features of the HAZ; (c-e) corrosion features of the TMAZ of RS and AS; (d) corrosion features of the SZ.

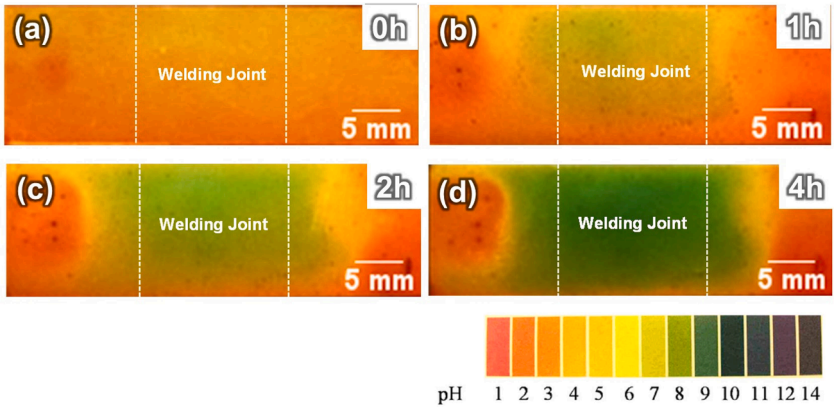

Fig. 12. . Results of agar-agar gel visualization test for the 2098-T351 alloy welded by FSW in 0.6 mol l^{-1} of NaCl.

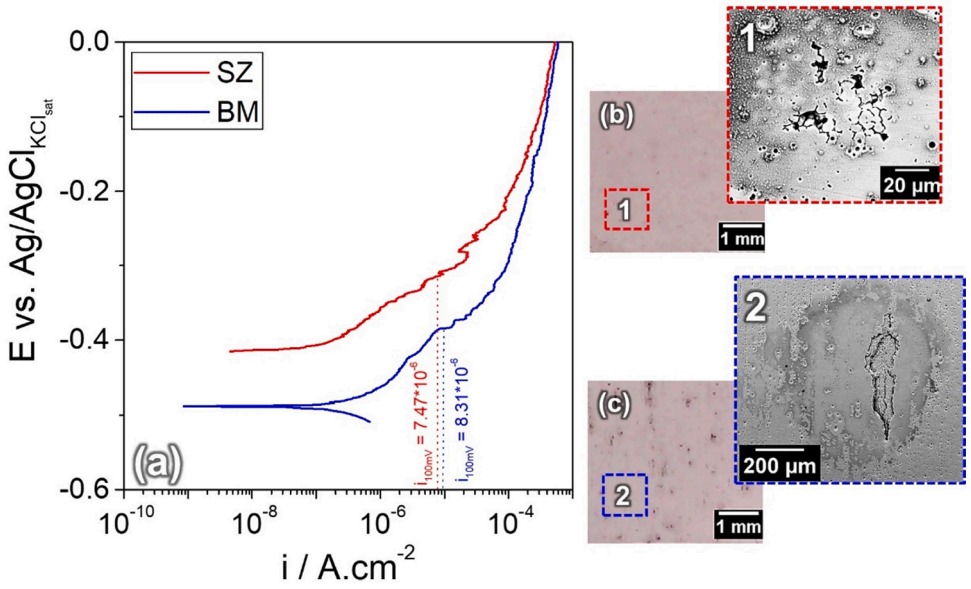

Fig. 13. . (a) Anodic polarization curves for different zones of AA2098-T351 welded by FSW after 30 min of immersion in 0.005 mol l^{-1} ^{1} of NaCl; (b) Anodic sites in SZ; (c) Anodic sites in BM.

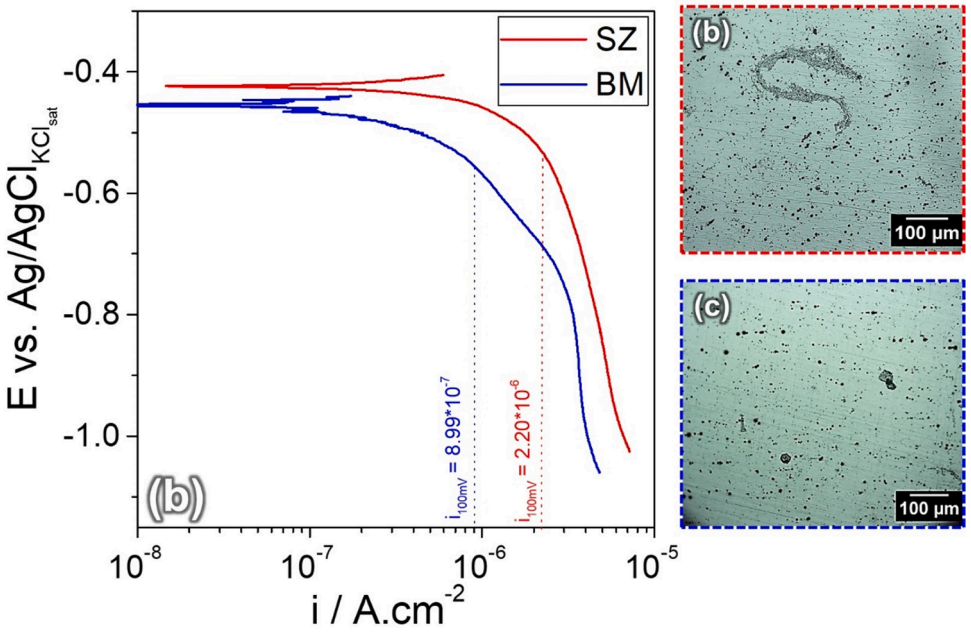

Fig. 14. . (a) Cathodic polarization curves comparing the BM and SZ of the AA2098-T351 2098-T351 alloy welded by FSW after 30 min of immersion in 0.005 mol l^{-1} of NaCl; (b) stir zone (SZ) and (c) base metal (BM).

Fig. 17 shows an inverse relationship between the mechanical properties and the average of the modulus of impedance with the distance from the weld centerline.

The impedance average was based on the values of impedance obtained after 16 h of immersion at a frequency of 10 Hz. The results showed that as the density of T1 phase decreases the corrosion resistance of the alloy increases. It is also observed that the WJ is the most resistant to corrosion among the welding zones evaluated. In the HAZ, the variability of impedance was higher than in the other zones. This result is related to the dependence of T1 phase partial dissolution and coarsening on temperature making this region highly heterogeneous.

To further analyze the corrosion behavior in the welded regions, SVET tests were performed, and the corresponding maps obtained after 12 h of immersion in a 0.005 mol L^{-1} NaCl solution are shown in Fig. 18.

These maps offer detailed insights into both macro- and micro-scale corrosion processes occurring in the different welding zones, correlating them with the observed electrochemical activity

The WJ exhibited predominantly cathodic activity when compared to the BM and HAZ. Anodic sites within the WJ showed lower current densities, which is consistent with the dissolution of phases that mitigate the effects of selective localized corrosion (SLC), (Fig. 18b). This reduced anodic activity is further influenced by the increased cathodic areas resulting from the fragmentation of micrometric particles caused by the tool movement during the welding process.

In contrast, the HAZ demonstrated significant anodic activity, particularly due to the presence of SLC sites (white arrows in Fig. 18a

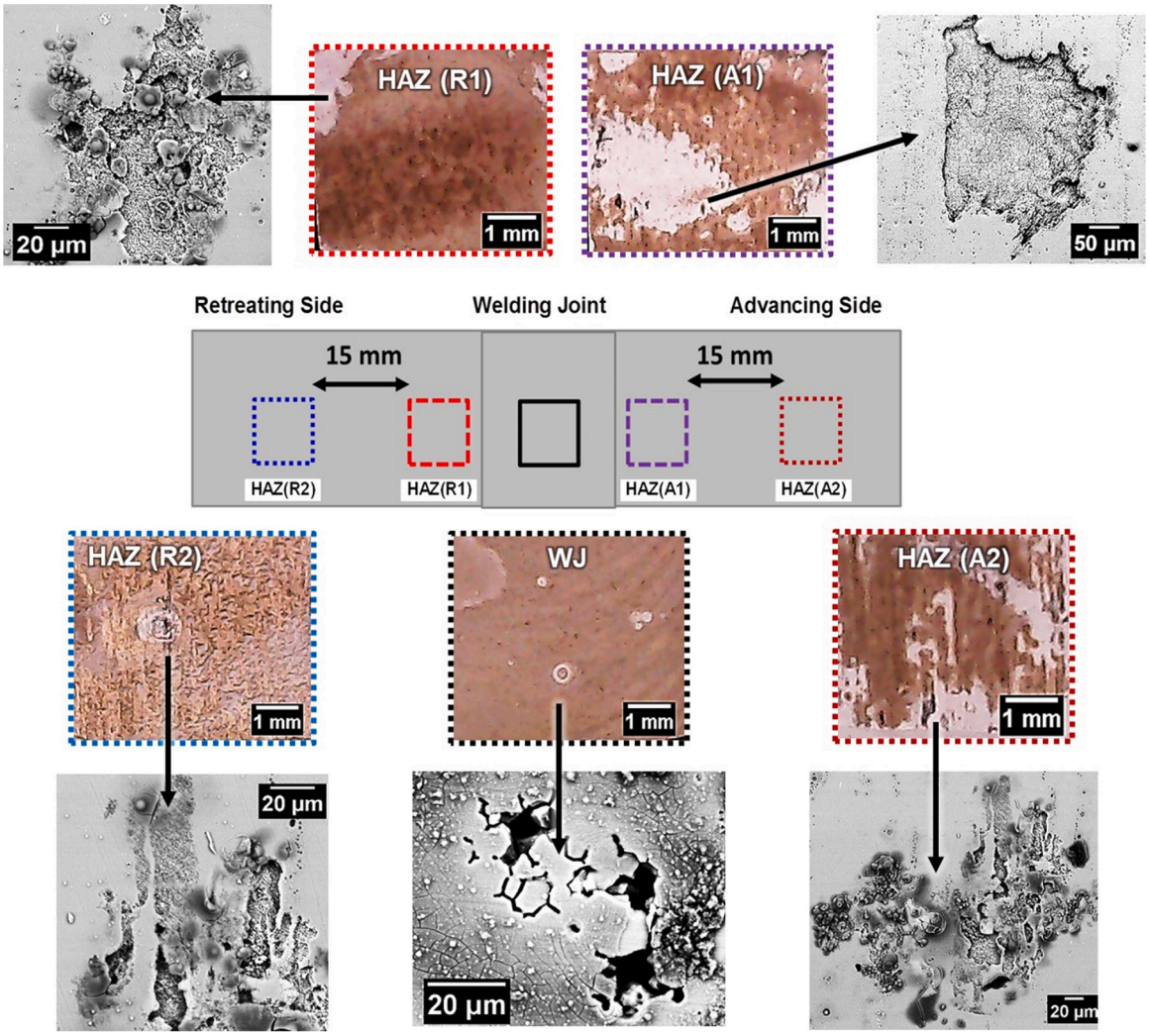

Fig. 15. . Optical microscopy of the different zones of the 2098-T351 alloy after 24 h of immersion in NaCl 0.005 mol. l^{-1}. (BM=Base metal, SZ=Stir zone, HAZA1 = Heat affected zone at advancing side near to the welding joint, HAZR1 = Heat affected zone at reatreating side near to the welding joint, HAZA2 = Heat affected zone at advancing side near to the base metal, HAZR2 = Heat affected zone at retreating side near to the base metal).

and c). These sites are more prominent in both the advancing side (AS) and retreating side (RS) of the HAZ, correlating with the microstructural changes induced by the welding process, such as phase coarsening and the formation of precipitate-free zones (PFZ). These microstructural transformations increase the susceptibility of the HAZ to localized corrosion mechanisms, as observed in the SVET maps.

The reduction of electrochemical activity in the WJ over the 12-hour immersion period (Fig. 18b) is linked to the formation of an oxide film, which acts as a protective barrier against further corrosion. Current densities in this region were approximately ten times lower than those observed at the galvanic coupling sites between the WJ and HAZ, reinforcing the protective role of the oxide film.

The SVET maps presented in Fig. 18 further corroborate the corrosion mechanisms previously discussed, particularly those identified in the immersion tests (Figs. 8-11) and the anodic polarization behavior (Fig. 13). The localized anodic activity observed in the HAZ through SVET (Fig. 18a) aligns with the earlier findings of severe localized corrosion (SLC) and intergranular attack, which were primarily attributed to the presence of the T1 phase and microstructural heterogeneities caused by the welding process.

In contrast, the reduced anodic current densities in the welding joint (Fig. 18b) correlate with the lower susceptibility to corrosion observed in immersion tests, where the dissolution of strengthening phases and the presence of oxide films were identified as key factors enhancing corrosion resistance. The microstructural characteristics that influenced these behaviors, such as the dissolution of precipitates and the formation of precipitate-free zones (PFZ), were thoroughly examined in Figs. 3-5, supporting the hypothesis that phase distribution plays a crucial role in corrosion susceptibility.

The macrographs in Fig. 18c, e, and f illustrate the surface condition of the FSW regions after SVET analyses. The surface corrosion morphology observed in Figs. 18c, e, and f, which depict the welded regions after SVET analysis, correlates well with the earlier observations presented in Fig. 15. The distribution of localized corrosion features across the weld zones in Fig. 15 provides additional confirmation of the anodic and cathodic behaviors detected through SVET mapping. Specifically, the higher susceptibility of the HAZ to severe localized corrosion (SLC), characterized by deep trenching and intergranular attack, is evident in both figures. The regions marked in Fig. 15, showing corrosion propagation along the HAZ, are consistent with the localized anodic sites identified in Fig. 18a and 18c, where the white arrows highlight areas of intense dissolution. Similarly, the more uniform and less aggressive corrosion morphology of the welding joint (SZ and TMAZ), observed in Fig. 15, is reinforced by the lower current densities recorded in the corresponding SVET maps (Fig. 18b).

By comparing these figures, it becomes evident that the microstructural differences induced by FSW directly influence the corrosion behavior, with the HAZ remaining the most vulnerable zone, while the

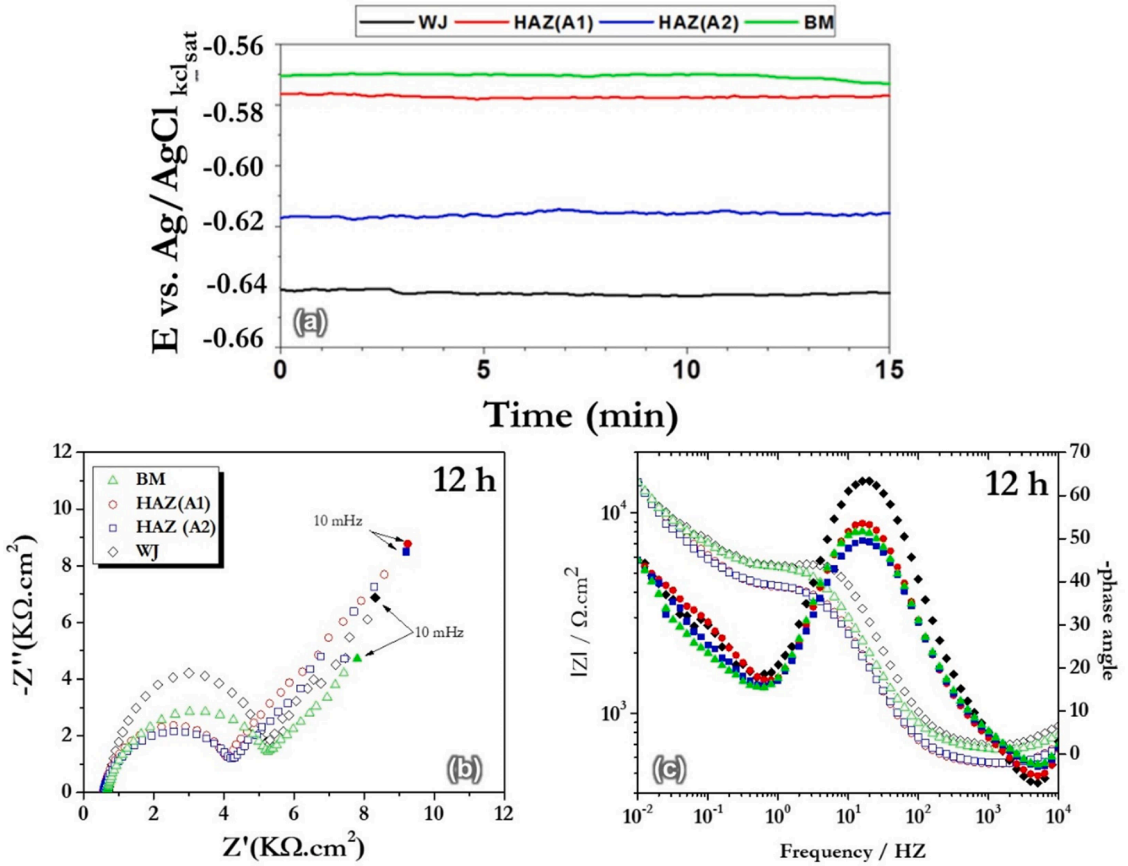

Fig. 16. . (a) 15 last minutes OCP values for the different welding zones before EIS measurements in 0.005 mol l^{-1} of NaCl; (c-d) EIS diagrams after 12 h of immersion.

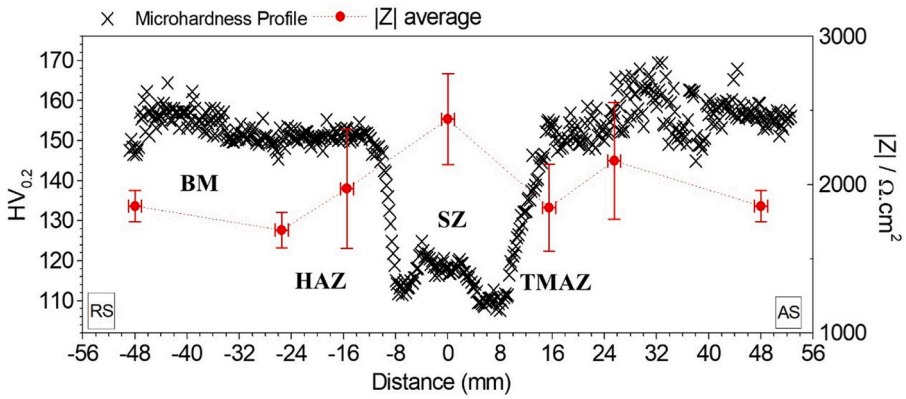

Fig. 17. . Relationship between microhardness profile and average of |Z|10 mHz obtained after 12 h of immersion in 0.005 mol l^{-1}.

SZ exhibits improved resistance due to phase dissolution and oxide film formation.

Based on the results obtained, Tale 1 shows a summary of the corrosion features observed according to each zone of the FSW weldment.

The results of this study showed that the welding process modifies the morphology of attack in the weld zones of the 2098-T351 alloy relative to the zone not affected by FSW, that is the BM. Surface observation after immersion showed different features of corrosion attack in the weldment, Table 1. Although differences were observed between SZ and BM using conventional electrochemical techniques, these techniques were not selective enough to show major differences in the corrosion resistance and/or mechanism between the welding affected zones (i.e. the SZ, HAZ and BM). One possible reason for the similar corrosion resistance for all tested zones is related to the fact that conventional electrochemical techniques provide mean values of current densities at the surface of the exposed area. On the other hand, localized electrochemical techniques are more appropriate for the study and evaluation of localized corrosion. In the case of SLC and surroundings, the anodic and cathodic currents can only be evaluated by local techniques.

The lower current densities obtained in the welding joint (TMAZ and SZ) compared with other zones suggest that the depth of corrosion penetration related to the SLC sites in the BM and HAZ is greater than that in the welding joint. These results agree with the reduction in T1 phase content in the welding joint as observed by TEM images and

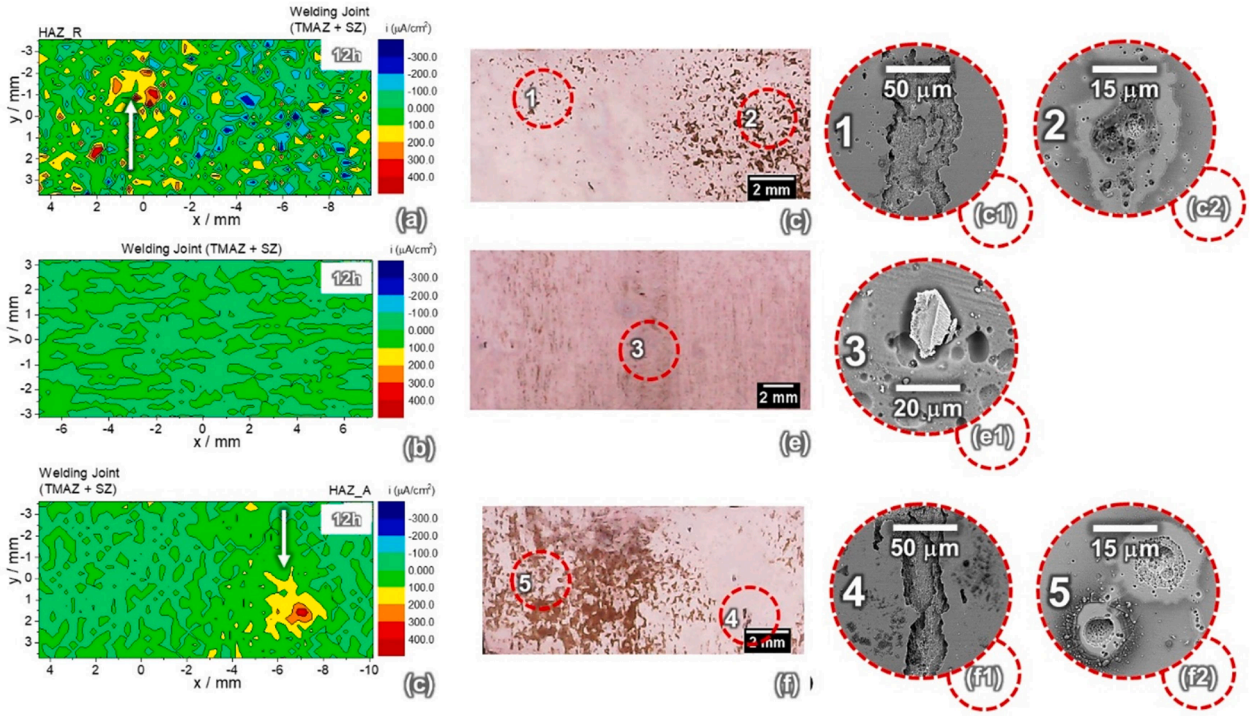

Fig. 18. . SVET maps (a, b, and c) and in situ observation (d, e, and f) of AA2098-T351 welded by FSW after 12 h of immersion in 0.005 mol L^{-1} NaCl. The dashed circles (c1–f2) correspond to SEM micrographs at higher magnification of the regions marked by dashed circles in (c), (e), and (f). The white arrows in (a) and (c) indicate sites of severe localized corrosion (SLC).

Table 1
. Summary of the different corrosion features observed in the welding zones of the 2098-T351 alloy welded by FSW.

Zone	Corrosion features
BM	Pit, trenching, intragranular SLC
HAZ	Pit, trenching, intragranular SLC
TMAZ	Pit, trenching, intragranular SLC, IGC
SZ	Pit, trenching, intergranular SLC

microhardness profile. In the case of the HAZ coupled to the welding joint, the higher susceptibility of the first zone to SLC compared to the latter results in small anodic areas associated with large cathodic ones, stimulating the penetration of corrosion attack in the SLC sites. This explains the higher currents for welding joints when coupled with the HAZ where SLC was seen. In this situation, the welding joint (TMAZ and SZ) is cathodically protected and the oxygen reduction reaction occurs predominantly on it. However, when the welding joint is tested independently, the lower susceptibility of this zone to SLC results in an evenly distributed attack. This elucidates the lower current densities associated with the welding joint and the even distribution of cathodic and anodic areas on this zone as compared to the BM and HAZ.

In the welding joint, segregations at the grain boundaries, reduction in T1 phase content and larger PFZ's explain the intergranular propagation of corrosion attack associated with the galvanic coupling. The lower current densities related to this zone and the even distribution of anodic and cathodic sites at the exposed surface support the premise that in the zones where the T1 phase is rare, the depth of penetration attack is shallower than in the zones where the T1 phase is abundant. However, the welding joint (TMAZ and SZ) is susceptible to localized corrosion, and, depending on the extension of the surface exposed to the corrosive environment, the morphology of attack changes. When galvanic coupling is established between the zones, the main corrosion mechanism observed in the SZ was related to the microgalvanic cells due to the micrometric particles and the matrix, as observed by the immersion test. However, when the zones are tested unconnectedly, all of them are susceptible to SLC. This result shows that depending on the area exposed to the aggressive media, the type and severity of corrosion attack changes.

4. Conclusions

FSW of the 2098-T351 alloy caused significant modifications in its microstructure and microhardness due to thermal and/or mechanical effects. The zones of different microstructures showed dissimilar electrochemical activities in 0.005 mol l^{-1} NaCl solution. SZ and TMAZ acted as cathodic regions relative to the HAZ and BM. This was shown by agar-agar and immersion tests. The corrosion mechanisms of the different zones also varied. The BM showed high susceptibility to severe localized corrosion (SLC); the HAZ also presented SLC but also localized corrosion attack related to micrometric constituent particles. The welding joint (SZ+TMAZ) exhibited susceptibility to intergranular corrosion and a lower tendency for severe localized corrosion (SLC). Galvanic coupling between different zones influenced the type of corrosion attack observed, in contrast to zones tested in isolation. The type and severity of corrosion attack was largely dependent on the area exposed to the aggressive medium and the galvanic coupling effect on the zones.

CRediT authorship contribution statement

João Victor de S. Araujo: Writing – original draft, Data curation, Conceptualization. **Mariana X. Milagre:** Writing – review & editing, Visualization, Methodology, Investigation, Formal analysis. **José Wilmar Calderón-Hernández:** Formal analysis. **Nathanael W. Morais:** Formal analysis. **Isolda Costa:** Writing – review & editing, Validation, Supervision, Project administration, Funding acquisition.

Declaration of competing interest

The authors declare that they have no known competing financial

interests or personal relationships that could have appeared to influence the work reported in this paper.

Acknowledgements

The authors would like to acknowledge CAPES (Capes/Cofecub No 806-14) and FAPESP (2013/13235-6) for their financial support. We also extend our gratitude to CAPES for the grant awarded to M.X. Milagre (99999.000332/2016-00).

References

[1] R. Nandan, T. Debroy, H.K.D.H. Bhadeshia, Recent advances in friction stir welding – process, weldment structure and properties, Prog. Mater. Sci. 53 (2008) 980–1023, https://doi.org/10.1016/j.pmatsci.2008.05.001.
[2] R.S. Mishra, Z.Y. Ma, Friction stir welding and processing, Mater. Sci. Eng. R: Rep. 50 (2005) 1–78, https://doi.org/10.1016/j.mser.2005.07.001.
[3] P.L. Threadgill, A.J. Leonard, H.R. Shercliff, P.J. Withers, Friction stir welding of aluminium alloys, Int. Mater. Rev. 54 (2009) 49–93, https://doi.org/10.1179/174328009X411136.
[4] R.W. Fonda, J.F. Bingert, Precipitation and grain refinement in a 2195 Al friction stir weld, Metall. Mater. Trans. A: Phys. Metall. Mater. Sci. 37 (2006) 3593–3604, https://doi.org/10.1007/s11661-006-1054-2.
[5] A. Steuwer, M. Dumont, J. Altenkirch, S. Birosca, A. Deschamps, P.B. Prangnell, P. J. Withers, A combined approach to microstructure mapping of an Al-Li AA2199 friction stir weld, Acta Mater. 59 (2011) 3002–3011, https://doi.org/10.1016/j.actamat.2011.01.040.
[6] J.C. Rao, E.J. Payton, C. Somsen, K. Neuking, G. Eggeler, A. Kostka, J.F. Dos Santos, Where Does the Lithium Go? - A Study of the Precipitates in the Stir Zone of a Friction Stir Weld in a Li-containing 2xxx Series Al Alloy, Adv. Eng. Mater. 12 (2010) 298–303, https://doi.org/10.1002/adem.200900284.
[7] A.K. Shukla, W.A. Baeslack, Study of process/structure/property relationships in friction stir welded thin sheet Al-Cu-Li alloy, Sci. Technol. Weld. Join. 14 (2009) 376–387, https://doi.org/10.1179/136217109X412409.
[8] A.K. Shukla, W.A. Baeslack, Study of microstructural evolution in friction-stir welded thin-sheet Al-Cu-Li alloy using transmission-electron microscopy, Scr. Mater. 56 (2007) 513–516, https://doi.org/10.1016/j.scriptamat.2006.11.028.
[9] C. Gao, Z. Zhu, J. Han, H. Li, Correlation of microstructure and mechanical properties in friction stir welded 2198-T8 Al-Li alloy, Mater. Sci. Eng. A 639 (2015) 489–499, https://doi.org/10.1016/j.msea.2015.05.038.
[10] P. Cavaliere, M. Cabibbo, F. Panella, A. Squillace, 2198 Al-Li plates joined by Friction Stir Welding: mechanical and microstructural behavior, Mater. Des. 30 (2009) 3622–3631, https://doi.org/10.1016/j.matdes.2009.02.021.
[11] S.M.O. Tavares, J.F. dos Santos, P.M.S.T. de Castro, Friction stir welded joints of Al-Li Alloys for aeronautical applications: butt-joints and tailor welded blanks, Theor. Appl. Fract. Mec. 65 (2013) 8–13, https://doi.org/10.1016/j.tafmec.2013.05.002.
[12] W. Li, R. Jiang, Z. Zhang, Y. Ma, Effect of rotation speed to welding speed ratio on microstructure and mechanical behavior of friction stir welded aluminum-lithium alloy joints, Adv. Eng. Mater. 15 (2013) 1051–1058, https://doi.org/10.1002/adem.201300147.
[13] E. Bousquet, A. Poulon-Quintin, M. Puiggali, O. Devos, M. Touzet, Relationship between microstructure, microhardness and corrosion sensitivity of an AA 2024-T3 friction stir welded joint, Corros. Sci. 53 (2011) 3026–3034, https://doi.org/10.1016/j.corsci.2011.05.049.
[14] J. Corral, E.A. Trillo, Y. Li, L.E. Murr, Corrosion of friction-stir welded aluminum alloys 2024 and 2195, J. Mater. Sci. Lett. (2000) 2117–2122, https://doi.org/10.1023/A:1026710422951.
[15] M. Jariyaboon, A.J. Davenport, R. Ambat, B.J. Connolly, S.W. Williams, D.A. Price, The effect of welding parameters on the corrosion behaviour of friction stir welded AA2024-T351, Corros. Sci. 49 (2007) 877–909, https://doi.org/10.1016/j.corsci.2006.05.038.
[16] C.P. de Abreu, I. Costa, H.G. de Melo, N. Pébère, B. Tribollet, V. Vivier, Multiscale Electrochemical Study of Welded Al Alloys Joined by Friction Stir Welding, J. Electrochem. Soc. 164 (2017) C645–C652, https://doi.org/10.1149/2.0391713jes.
[17] J.B. Lumsden, M.W. Mahoney, G. Pollock, C.G. Rhodes, Intergranular corrosion following friction stir welding of aluminum alloy 7075-T651, Corrosion 55 (1999) 1127–1135, https://doi.org/10.5006/1.3283950.
[18] W. Hu, E.I. Meletis, Corrosion and environment-assisted cracking behavior of friction stir welded Al 2195 and Al 2219 alloys, Mater. Sci. Forum 331–337 (2000) 1683–1688, https://doi.org/10.4028/www.scientific.net/MSF.331-337.1683.
[19] C.S. Paglia, R.G. Buchheit, A look in the corrosion of aluminum alloy friction stir welds, Scr. Mater. 58 (2008) 383–387, https://doi.org/10.1016/j.scriptamat.2007.10.043.
[20] V. Proton, J. Alexis, E. Andrieu, J. Delfosse, M.C. Lafont, C. Blanc, Characterisation and understanding of the corrosion behaviour of the nugget in a 2050 aluminium alloy Friction Stir Welding joint, Corros. Sci. 73 (2013) 130–142, https://doi.org/10.1016/j.corsci.2013.04.001.
[21] J. Kang, Z. Feng, G.S. Frankel, J. Li, G. Zou, A. Wu, Effect of precipitate evolution on the pitting corrosion of friction stir welded joints of an Al-Cu alloy, Corrosion 72 (2016) 719–731, https://doi.org/10.5006/2049.
[22] J.W.X. Zhang, B. Liu, X. Zhou, Z.T. Chen, F.L. Luo, Z. Sun, Corrosion behavior of friction stir welded 2A97 Al-Cu-Li alloy, Corrosion 9312 (2017) 2418, https://doi.org/10.5006/2418.
[23] G. T, V.G.F. Zucchi, Pitting and stress corrosion cracking resistance of friction stir welded AA 5083, Mater. Corros. 52 (2001) 853–859, https://doi.org/10.1002/1521-4176(200111)52:11<853::AID-MACO853>3.0.CO;2-1.
[24] D. Sidane, E. Bousquet, O. Devos, M. Puiggali, M. Touzet, V. Vivier, A. Poulon-Quintin, Local electrochemical study of friction stir welded aluminum alloy assembly, J. Electroanal. Chem. 737 (2015) 206–211, https://doi.org/10.1016/j.jelechem.2014.06.025.
[25] Y. Peng, C. Shen, Y. Zhao, Y. Chen, Comparison of Electrochemical Behaviors between FSW and MIG Joints for 6082 Aluminum Alloy, Xiyou Jinshu Cailiao Yu Gongcheng/Rare Metal Mater. Eng. 46 (2017) 344–348, https://doi.org/10.1016/S1875-5372(17)30092-9.
[26] A. Davoodi, Z. Esfahani, M. Sarvghad, Microstructure and corrosion characterization of the interfacial region in dissimilar friction stir welded AA5083 to AA7023, Corros. Sci. 107 (2016) 133–144, https://doi.org/10.1016/j.corsci.2016.02.027.
[27] J.C.B. Bertoncello, S.M. Manhabosco, L.F.P. Dick, Corrosion study of the friction stir lap joint of AA7050-T76511 on AA2024-T3 using the scanning vibrating electrode technique, Corros. Sci. 94 (2015) 359–367, https://doi.org/10.1016/j.corsci.2015.02.029.
[28] U. Donatus, G.E. Thompson, X. Zhou, J. Wang, A. Cassell, K. Beamish, Corrosion susceptibility of dissimilar friction stir welds of AA5083 and AA6082 alloys, Mater. Charact. 107 (2015) 85–97, https://doi.org/10.1016/j.matchar.2015.07.002.
[29] C.S.C. Machado, J.V.S. Araujo, J.W.C. Hernández, M.X. Milagre, O.M.P. Ramirez, H.G. de Melo, S. Farooq, I. Costa, Understanding the effect of corrosion resistance in welded aa2198-t8 alloy: microstructural-electrochemical insights, Mater. Corros. (2024), https://doi.org/10.1002/maco.202414545.
[30] M.X. Milagre, U. Donatus, N.V. Mogili, C.S.C. Machado, J.V.S. Araujo, R.M.P. Silva, R.A. Antunes, S. Farooq, I. Costa, Quantifying intergranular corrosion susceptibility in AA2098-T351 weldments through friction stir welding, Mater. Corros. 75 (2024) 1359–1372, https://doi.org/10.1002/maco.202314245.
[31] M.E. Orazem, B. Tribollet, Electrochemical Impedance Spectroscopy, Electrochem. Impedance Spectrosc. (2008) 1–523, https://doi.org/10.1002/9780470381588.
[32] M.X. Milagre, N.V. Mogili, U. Donatus, R.A.R. Giorjão, M. Terada, J.V.S. Araujo, C. S.C. Machado, I. Costa, On the microstructure characterization of the AA2098-T351 alloy welded by FSW, Mater. Charact. 140 (2018) 233–246, https://doi.org/10.1016/j.matchar.2018.04.015.
[33] U. Donatus, M. Terada, C. Ramirez, F. Martins, A. Fatima, S. Bugarin, I. Costa, On the AA2198-T851 alloy microstructure and its correlation with localized corrosion behaviour, Corros. Sci. 131 (2018) 300–309, https://doi.org/10.1016/j.corsci.2017.12.001.
[34] J.V. de Sousa Araujo, U. Donatus, F.M. Queiroz, M. Terada, M.X. Milagre, M.C. de Alencar, I. Costa, On the severe localized corrosion susceptibility of the AA2198-T851 alloy, Corros. Sci. 133 (2018) 132–140, https://doi.org/10.1016/j.corsci.2018.01.028.
[35] Y. Ma, X. Zhou, W. Huang, G.E. Thompson, X. Zhang, C. Luo, Z. Sun, Localized corrosion in AA2099-T83 aluminum-lithium alloy: the role of intermetallic particles, Mater. Chem. Phys. 161 (2015) 201–210, https://doi.org/10.1016/j.matchemphys.2015.05.037.
[36] Y. Ma, X. Zhou, Y. Liao, Y. Yi, H. Wu, Z. Wang, W. Huang, Localised corrosion in AA2099-T83 aluminium-lithium alloy: the role of grain orientation, Corros. Sci. 107 (2015) 41–48, https://doi.org/10.1016/j.corsci.2016.02.018.
[37] U. Donatus, L.O. Berbel, I. Costa, Qualitative use of potentiodynamic polarization and anodic hydrogen evolution in the assessment of corrosion susceptibility in AA2198-T851 Al – Cu – Li alloy, Mater. Corros. (2018) 1–14, https://doi.org/10.1002/maco.201810108.
[38] J.F. Li, C.X. Li, Z.W. Peng, W.J. Chen, Z.Q. Zheng, Corrosion mechanism associated with T1 and T2 precipitates of Al-Cu-Li alloys in NaCl solution, J. Alloys Compd. 460 (2008) 688–693, https://doi.org/10.1016/j.jallcom.2007.06.072.
[39] G.E.S.R.G. Buchheit Jr., J.P. Moran, Localized corrosion behavior of alloy 2090-the role of microstructural heterogeneity, Corrosion 46 (1990) 610–617.
[40] A. Boag, A.E. Hughes, A.M. Glenn, T.H. Muster, D. McCulloch, Corrosion of AA2024-T3 Part I: localised corrosion of isolated IM particles, Corros. Sci. 53 (2011) 17–26, https://doi.org/10.1016/j.corsci.2010.09.009.
[41] A.E. Hughes, A. Boag, A.M. Glenn, D. McCulloch, T.H. Muster, C. Ryan, C. Luo, X. Zhou, G.E. Thompson, Corrosion of AA2024-T3 Part II: co-operative corrosion, Corros Sci 53 (2011) 27–39, https://doi.org/10.1016/j.corsci.2010.09.030.
[42] A.M. Glenn, T.H. Muster, C. Luo, X. Zhou, G.E. Thompson, A. Boag, A.E. Hughes, Corrosion of AA2024-T3 Part III: propagation, Corros. Sci. 53 (2011) 40–50, https://doi.org/10.1016/j.corsci.2010.09.035.
[43] R.G. Buchheit, M.A. Martinez, L.P. Montes, Evidence for Cu ion formation by dissolution and dealloying the al2cumg intermetallic compound in rotating ring-disk collection experiments, J. Electrochem. Soc. 147 (2000) 119–124, https://doi.org/10.1149/1.1393164.
[44] L. Reich, M. Murayama, K. Hono, Evolution of Ω phase in an Al–Cu–Mg–Ag alloy—A three-dimensional atom probe study, Acta Mater. 46 (1998) 6053–6062, https://doi.org/10.1016/S1359-6454(98)00280-8.
[45] M. Murayama, K. Hono, Role of Ag and Mg on precipitation of T1phase in an Al-Cu-Li-Mg-Ag alloy, Scr. Mater. 44 (2001) 701–706, https://doi.org/10.1016/S1359-6462(00)00651-5.

[46] P.S. Chen, B.N. Bhat, Time-Temperature-Precipitation Behavior in AI-Li Alloy 2195. Technical Report, 2002.
[47] C. Luo, S.P. Albu, X. Zhou, Z. Sun, X. Zhang, Z. Tang, G.E. Thompson, Continuous and discontinuous localized corrosion of a 2xxx aluminium-copper-lithium alloy in sodium chloride solution, J. Alloys Compd. 658 (2016) 61–70, https://doi.org/10.1016/j.jallcom.2015.10.185.
[48] J.V. de Sousa Araujo, A. de F. Santos Bugarin, U. Donatus, C. de S.C. Machado, F. M. Queiroz, M. Terada, I. Costa, Thermomechanical treatment and corrosion resistance correlation in the AA2198 Al–Cu–Li alloy, Corros. Eng., Sci. Technol. 54 (2019) 575–586.